Materials Horizons

Accepted Manuscript

This article can be cited before page numbers have been issued, to do this please use: F. Shen, H. Zhou, F. Hu, J. Wang, S. Deng, B. Wang, H. Wu, Q. Huang, J. Wang, J. Chen, L. He, J. Hao, Z. Yu, F. Liang, T. Liang, J. Sun and B. Sheng, *Mater. Horiz.*, 2019, DOI: 10.1039/C9MH01602C.

ROYAL SOCIETY OF CHEMISTRY

rsc.li/materials-horizons

View Article Online
DOI: 10.1039/C9MH01602C

New Concepts:

Negative thermal expansion (NTE) has emerged as one of intense research topics. Chemical modification and particle size effect have been regarded as effective means to tune the NTE behavior. However, the amplitude and temperature region of the NTE are usually limited by crystallographic contribution. Here, we report a new way to tune the NTE behavior, which involves the lattice distortion dominated by the magnetic structure in MnM'Ge-based (M' =Ni, Co) alloys. The large lattice distortion caused by cone-spiral magnetic ordering in Fe-doped MnNiGe motivates cleavage breaking and induces texture effect, which greatly enhances the NTE. The achieved maximal linear NTE is 3.3 times larger than that of corresponding average crystallographical contribution, and exceeds almost all NTE materials reported to date. In contrast, the less lattice distortion in MnCoGeIn with linear FM ordering makes it lack texture forming ability, and the maximal NTE never exceeds crystallographic contribution. It is the first time to tune the NTE behavior relying on the lattice distortion dominated by magnetic structure and the induced texture effect, which helps to break through the restriction of crystallographic contribution and achieves a giant NTE behavior. The present study provides a new strategy for exploring the adjustable NTE behavior.

View Article Online
DOI: 10.1039/C9MH01602C

Cone-spiral magnetic ordering dominated lattice distortion and giant negative thermal expansion in Fe-doped MnNiGe compounds

Received 00th January 20xx,
Accepted 00th January 20xx

DOI: 10.1039/x0xx00000x

Feiran Shen,[#abd] Houbo Zhou,[#ab] Fengxia Hu,*[abc], Jiantao Wang,[a,b] Sihao Deng,[d] Baotian Wang,[d] Hui Wu,[e] Qingzhen Huang,[e] Jing Wang,*[abf] Jie Chen,[d] Lunhua He,*[acd], Jiazheng Hao,[a] Zibing Yu,[ab] Feixiang Liang,[ab] Tianjiao Liang,[d] Jirong Sun,[abc] and Baogen Shen*[abc]

Negative thermal expansion (NTE) has emerged as one of intense research topics to meet the demands of precision industry for compensating positive thermal expansion (PTE) properties. The adjustment of NTE behavior is the key for tailoring thermal expansion. Chemical modification and particle size effect have been regarded as effective means to tune NTE behavior, and the crystallographic contribution is usually the upper limit of NTE. Here, we report a new way to tune the NTE behavior involving lattice distortion dominated by magnetic structure in hexagonal MnM'Ge-based (M': Ni, Co) alloys. The achieved maximal linear NTE reaches $\Delta L/L \sim -23690 \times 10^{-6}$ ($\bar{\alpha} = -121.5 \times 10^{-6}$/K) in a temperature interval as wide as ~195K (80-275K) for Fe-doped MnNiGe alloys. This value is 3.3 times larger than that of corresponding average crystallographical contribution, and exceeds almost all NTE materials reported to date. Neutron powder diffraction and first-principles calculations were carried out. The results revealed that the Fe-doped MnNiGe shows an incommensurate cone-spiral magnetic ordering, and the lattice distortion during phase transition is more significant than that of MnCoGeIn with a linear ferromagnetic ordering. The larger lattice distortion favors cleavage breaking of hexagonal phase along c-axis. As a result, texture effect along (110) crystal plane occurs during molding process, which greatly enhances the amplitude of isotropic in-plane linear NTE. The present study provides a new strategy for exploring adjustable NTE behavior.

Introduction

It is well known that most materials exhibit positive thermal expansion (PTE) properties. Although the length change caused by PTE is only 10^{-5} to 10^{-6}, this magnitude of change can greatly affect the performance of some devices or instruments, especially in some precision industrial fields, such as printed circuit boards, optical fiber reflective grating devices, and high-precision optical mirrors. The undesired PTE behavior of conventional materials can be effectively modified by mixing with a negative thermal expansion (NTE) material. Therefore, NTE has emerged as one of intense research topics to meet the demands of precision industry. However, the applications making the precise devices usually need good matched coefficient of thermal expansion (CTE) between different components. The adjustment of NTE behavior, which includes the amplitude and the temperature region of NTE, becomes the key of NTE research. Currently, chemical modification has been regarded as an effective method to tune NTE behavior in many NTE materials,[1] such as ZrW_2O_8-based compounds,[2-4] ScF_3-based compounds,[5,6] $PbTiO_3$-based compounds,[7-9] antiperovskite manganese nitrides,[10-14] $La(Fe,Si)_{13}$-based compounds,[15,16] cubic Laves phase $Tb(Co,Fe)_2$[17] and $BiNO_3$.[18] Additionally, particle size effect can also control the thermal expansion behavior through interface effects or defects in some cases, such as CuO,[19] $PbTiO_3$–$BiFeO_3$ Perovskite,[20] antiperovskite $Mn_3Cu_{0.5}Ge_{0.5}N$,[21] PtNi,[22] semimetal bismuth,[23] TiO_2[24] and ScF_3.[25] Although the NTE behavior can be tuned by these two methods, the amplitude and temperature region of NTE is normally limited by the crystallographic contribution whatever the dominated mechanism is phonon induced type,[2-6,23-25] such as tension effect, or electronic transition induced one, such as magnetic, ferroelectric, or charge order.[7-22] In other words, it's hard to obtain a NTE that exceeds lattice contribution. One exception is the giant NTE reported recently in the reduced layered ruthenate.[26,27] The maximal linear thermal expansion, $\Delta L/L \sim 22333 \times 10^{-6}$, largely exceeds the crystallographic contribution during the Mott metal–insulator phase transition. The cause was related to the change of elastic properties and morphology by the reduction of oxygen.[27]

Ternary metallic compounds MM'X (M, M' = Transition element, X = Main element) with proper components undergo a martensitic structural transition from hexagonal Ni_2In-type austenite (space group $P6_3/mmc$) to TiNiSi-type orthorhombic martensite (space group Pnma) on cooling. During the transition, hexagonal lattice expands along c-axis (c_H) and contracts along a-axis (a_H), accompanying with significant anisotropic unit-cell volume expansion.[28] Hence this type of materials provides excellent platform for exploring novel performance of NTE. For instance, via bonding the

[a.] Institute of Physics, Chinese Academy of Sciences, Beijing 100190, China.E-mail: fxhu@iphy.ac.cn, lhhe@iphy.ac.cn, wangjing@iphy.ac.cn, shenbg@iphy.ac.cn.
[b.] School of Physical Sciences, University of Chinese Academy of Sciences, Beijing 101408, China.
[c.] Songshan Lake Materials Laboratory, Dongguan, Guangdong 523808, China.
[d.] Spallation Neutron Source Science Center, Dongguan 523803, China.
[e.] NIST Center for Neutron Research, National Institute of Standards and Technology, Gaithersburg, Maryland 20899, USA.
[f.] Fujian Innovation Academy, Chinese Academy of Sciences, Fuzhou, Fujian 350108, China.

†Electronic Supplementary Information (ESI) available: sample preparation, characterization, computational method, magnetic and crystal structure analysis, first-principles calculations, texture analysis, and supplementary table and figures. See DOI: 10.1039/x0xx00000x

polycrystalline powders and introducing residual stress to impact phase transition,[29] isotropic NTE with linear expansion as large as $\Delta L/L \sim -10213 \times 10^{-6}$ (~ 93% of the crystallographic value $\Delta V/V$ = -3.9%[30]) in a wide temperature range was obtained in the MnCoGe-based compounds, which surpasses the performance of most NTE materials.

For the MM'X (M=Mn) alloys, the austenite usually displays ferromagnetic (FM) properties, but various magnetic ground states appear in martensite. During phase transition, the arrangement of Mn atoms (the main carriers of magnetic moment) changes from straight alignment in austenite to polygonal chains in martensite (Fig. 1a,b). The interatomic distances between adjacent Mn atoms (d_1, d_2) are therefore changed[31] (see Fig. S1 in supporting material), resulting in rich magnetic ground states in martensite because the magnetic coupling is extremely sensitive to the Mn-Mn interatomic distances.[32,33] For example, the stoichiometric MnNiGe[34] and MnCoGe[35] display antiferromagnetic (AFM) and FM nature in martensite, respectively, where the only difference is the element on M' site, i.e. Co and Ni, which are neighbors in periodic table and have almost the same atomic radius. However, the lattice symmetry and interatomic distance of MnCoGe and MnNiGe are pronouncedly affected by their distinct magnetic couplings.

The stoichiometric MnNiGe shows a martensitic structural transition around $T_S \sim 420$ K, and the martensite displays spiral AFM structure with Neel temperature T_N at ~ 356 K.[34] By optimizing compositions, concurrent magnetic and structural transitions emerge as either Mn or Ni site is substituted by Fe,[36] hence giant magnetocaloric effect (MCE) has been reported. Although the negative expansion during phase transition (such as $\Delta V/V \sim$ -2.68% for $Mn_{0.86}Ni_{0.14}FeGe$)[36] is smaller than that of MnCoGe-based alloys ($\Delta V/V \sim$ -3.9% for $MnCoGe_{0.99}In_{0.01}$), [30] our neutron studies reveal that the Fe-doped MnNiGe with a cone-spiral magnetic structure shows a larger change of lattice distortion than that of MnCoGeIn with a linear FM structure during the transition (see Fig. S2). The large lattice distortion favors cleavage breaking during pulverization process, hence strong texture can be produced under pressure during molding process. By utilizing the magnetic structure controlled lattice distortion, giant NTE is achieved in Fe-doped MnNiGe. The maximal linear expansion reaches $\Delta L/L \sim -23690 \times 10^{-6}$ in a wide temperature window of 195K (80-275K), which exceeds the performance of almost all other NTE materials reported to date.

Results and Discussion

The Fe-doped MnNiGe alloys were synthesized by means similarly to Ref.[29] (supporting material I). To know the details of magnetic structure and lattice symmetry during phase transition, we performed variable temperature neutron powder diffraction (NPD) studies for $Mn_{1-x}Fe_xNiGe$ (x = 0.11, 0.13) and x-ray diffraction (XRD) for $MnNi_{1-y}Fe_yGe$ (y = 0.2, 0.23) and $Mn_{1-x}Fe_xNiGe$ (x = 0.09) (supporting material II). The refined results were given in Table S1 together with those of $MnCoGe_{0.99}In_{0.01}$.[30] The NPD refinements indicate a spiral-type incommensurate magnetic structure with the spiral axis parallel to a-axis for the martensite of $Mn_{0.87}Fe_{0.13}NiGe$. The magnetic reflections are indexed by the propagation vector k = [0.173(3), 0, 0]. The magnetic moment localizes on Mn sites with μ(Mn, Fe) = 2.66(1) μ_B, and the angle from a-axis is 70° at 200 K, showing a canted FM nature (here we assume that the Fe and Mn randomly occupy the same sites). In contrast, the $MnCoGe_{0.99}In_{0.01}$ with Co shows a linear FM structure in martensite with μ(Mn) = 2.74(5) μ_B and μ(Co) = 0.78(6) μ_B at 250 K (see Fig. 1c and Fig. 1d, and the details in Table S1).

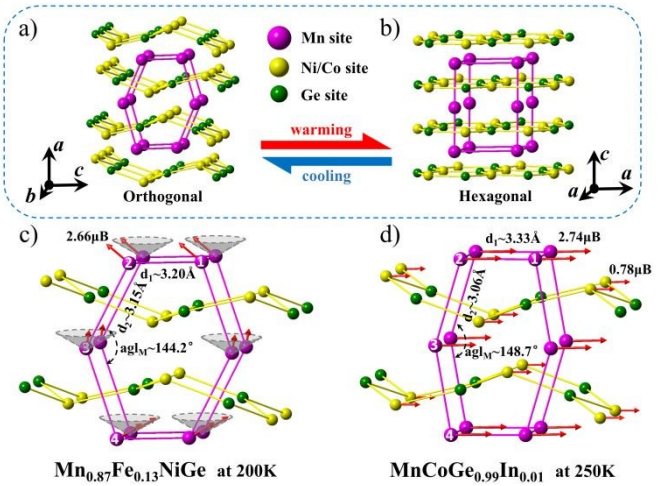

Fig. 1 a)-b) Sketches of orthorhombic and hexagonal structure of MnNiGe/MnCoGe, where the change of unit cell (magenta lines enclosed) and atomic chains can be clearly identified. c)-d) Fragments of the cone-spiral magnetic structure ($Mn_{0.87}Fe_{0.13}NiGe$) and linear FM ($MnCoGe_{0.99}In_{0.01}$) structures viewed along b axes with selected distances labeled in Å, the Mn1-Mn2 distance d_1 along c-axis, the Mn2-Mn3 distance d_2, and the angle agl_M of Mn2-Mn3-Mn4 atomic chain are indicated.

For such TiNiSi-type martensites, magnetic structure results from the competition between direct exchange of Mn1-Mn2 (d_1) and superexchange of Mn2-Mn3 (d_2) (Fig. 1c, d), while the former plays a dominant role.[32,33,37] Density functional theory (DFT)[32,33] calculations revealed that the magnetic ground state critically depends on the d_1 length. For $d_1 \leq 2.5$ Å, the close distance between Mn atoms leads to a strong overlap of 3d orbitals, and no magnetic ground state is stable due to the broad 3d hybrid bands. As the d_1 length increases, the overlap of the 3d orbitals of Mn becomes smaller, resulting in more localized 3d electrons and enhanced exchanges between Mn atoms. For 2.5 Å ≤ d_1 ≤ 2.9 Å, FM ground state shows lower energy, while for 2.9 Å ≤ d_1 ≤ 3.3 Å, AFM state shows lower energy. With further increasing d_1 length to $d_1 \geq 3.3$ Å, the FM state prevails again. These calculations were experimentally verified by several members of the MM'X family, such as MnNiSi (FM, d_1=2.78Å),[37] MnCoP(FM, d_1=2.88Å),[32] MnNiGe(AFM, d_1=3.20Å),[34] and MnCoGeIn(FM, d_1=3.33Å, Fig.1d).[30] But, during the calculations, collinear magnetic structure was considered.[32,33]

To demonstrate the stability of spiral AFM structure in MnNiGe alloy, we constructed a collinear AFM model and a spiral AFM model with a six unit cell period along the *a*-axis

based on the NPD data. The total energy were calculated by first-principles calculations with PW91 generalized gradient approximation.[38,39] (see computational details given in supporting materials I). The results (Fig. 2a) indicate that the total energy of the spiral AFM structure (-78.557 eV/f.u.) is lower than that of the collinear AFM (-78.272 eV/f.u.), suggesting that the spiral AFM ground state is more stable for MnNiGe.

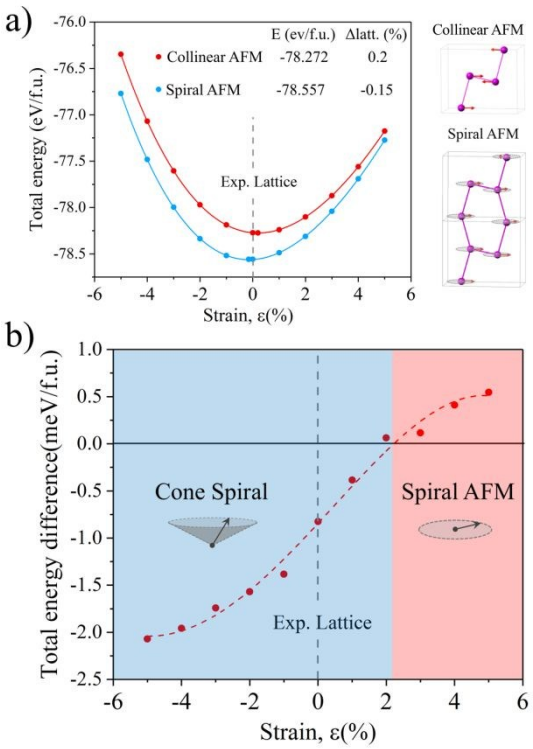

Fig 2. a) Total energy per formula unit of the MnNiGe as a function of the lattice strain for the spiral AFM and collinear AFM states. Right panel shows the sketch of collinear AFM and spiral AFM magnetic strcuture. b) Difference between the total energies of cone-spiral and spiral AFM states in $Mn_{0.87}Fe_{0.13}NiGe$ as a function of the lattice strain. The cone-spiral magnetic configuration becomes stable when $\Delta E<0$.

For the present $Mn_{0.87}Fe_{0.13}NiGe$, d_1 is 3.20Å, the same as those in the stoichiometric MnNiGe,[34] which should favour the spiral AFM coupling. However, the substitution of Mn with Fe introduces FM coupling in Fe–6Mn configurations,[36] which can help to establish a cone-spiral magnetic coupling. To confirm the stability of the cone-spiral magnetic structure in $Mn_{0.87}Fe_{0.13}NiGe$, we further calculated the total energy in both cone-spiral state and spiral AFM state, where the atomic position, i.e. structural symmetry, refined from NPD data was taken into account. The energy difference ($\Delta E=E_{cone\text{-}spiral}-E_{spiral\text{-}AFM}$) per formula unit is plotted in Fig. 2b with an isotropic lattice strain change from -5% to +5% related to the experimental lattice parameters. The results indicate that the cone-spiral magnetic state is more stable than the spiral AFM noting an energy gain of 0.8 meV/f.u. with the experimental lattice parameters (ε = 0%).

For lattice distortion relative to magnetic structure (Fig.1c,d), we choose a representative composition $Mn_{0.87}Fe_{0.13}NiGe$ and compare it to $MnCoGe_{0.99}In_{0.01}$ with linear FM structure. Due to the distinct magnetic coupling, the differences of d_1 and d_2 between the two alloys reach 3.61% and 2.60%, respectively, and the agl_M (144.3°) of Mn2-Mn3-Mn4 atomic chain in $Mn_{0.87}Fe_{0.13}NiGe$ is smaller than that (148.6°) in $MnCoGe_{0.99}In_{0.01}$ by 2.89% (Fig. S1, Table S1). Hence different lattice symmetries appear in martensite for the two alloys, which are evidently displayed in Fig. 1c,d. As seen from Table S1, the d_1, d_2, agl_M, as well as lattice parameters indicate that all the Fe-doped MnNiGe alloys show larger lattice distortions than $MnCoGe_{0.99}In_{0.01}$ during the martensitic transition.

To quantify the lattice distortion, we define a numeral parameter, Δ_{ani}, as following,

$$\Delta_{ani} = \sqrt{\frac{1}{3}\cdot[(\Delta a/a - \Delta l/l)^2 + (\Delta b/b - \Delta l/l)^2 + (\Delta c/c - \Delta l/l)^2]} \quad (1)$$

where $\Delta a/a = (c_H - a_O)/c_H$, $\Delta b/b = (a_H - b_O)/b_O$, $\Delta c/c = (a_H - c_O)/a_H$ denote the change ratio of lattice parameters across the transition between hexagonal (H) and orthorhombic (O) phases, and $\Delta l/l = (\Delta V/V)/3$ ($\Delta V/V$ represents the change of unit-cell volume). The obtained Δ_{ani} is 8.68%, 8.35%, 8.40%, 8.51%, and 8.27% for $Mn_{0.87}Fe_{0.13}NiGe$, $MnNi_{0.8}Fe_{0.2}Ge$, $MnNi_{0.77}Fe_{0.23}Ge$, $Mn_{0.91}Fe_{0.09}NiGe$, and $Mn_{0.89}Fe_{0.11}NiGe$, respectively (Table S1), which show similar cone-spiral magnetic structure (see details in supporting material II, Fig. S3, S4, and S5). In contrast, the $MnCoGe_{0.99}In_{0.01}$ with linear FM structure shows a Δ_{ani} about 7.49%, smaller than those of Fe-doped MnNiGe by 12% in average. The larger lattice distortion motivates cleavage breaking during pulverization process, and strong texture appears under pressure. As a result, NTE with giant linear $\Delta L/L$ is achieved in the Fe-doped MnNiGe alloys.

Fig. 3a shows the linear thermal expansion $\Delta L/L$ measured using high-resolution strain gauge from 390 K down to 80 K for the bonded samples with different particle sizes. The $\Delta L/L$ behaves in-plane isotropy (Fig. 3c). For $Mn_{0.87}Fe_{0.13}NiGe$, $MnNi_{0.8}Fe_{0.2}Ge$, $MnNi_{0.77}Fe_{0.23}Ge$, and $Mn_{0.91}Fe_{0.09}NiGe$, the particle sizes before bonding are 60~80 μm, 20~50 μm, 20~40 μm, and 10~20 μm (Fig. 3b), and the measured maximal $\Delta L/L$'s reach 23690, 17416, 16172, and 9171×10^{-6} in the temperature interval 195K (80-275K), 162K (180-342K), 186K (132-318K), and 138K (194-332K), and hence the corresponding average linear NTE coefficients are $\bar{\alpha}$ ~ -121.5, -107.5, -86.9, and -66.5×10^{-6}/K, respectively (Table S1). Note that the measured $\Delta L/L$ ~ 23690×10^{-6} for $Mn_{0.87}Fe_{0.13}NiGe$ has not reached the maximum at 80 K. It means the actual $\Delta L/L$ should be larger. Even so, the maximal $\Delta L/L$ ~ 23690×10^{-6} and the corresponding NTE coefficient $\bar{\alpha}$ ~ -121.5×10^{-6}/K over ~ 195 K interval have exceeded almost all NTE materials reported previously. For example, these performances reach or even surpass the $\Delta L/L$ ~ 22333×10^{-6} and the maximal $\bar{\alpha}$ ~ 115×10^{-6}/K (over the nearly equivalent interval of ~ 200 K) of the reduced layered ruthenate, the maximal NTE reported to date.[27] Moreover, the present $\Delta L/L$ ~ 23690×10^{-6} is more than 2 times larger than that ($\Delta L/L$ ~ 10213×10^{-6}) of the bonded $MnCoGe_{0.99}In_{0.01}$,[29] and the corresponding NTE coefficient $\bar{\alpha}$ ~ -121.5×10^{-6}/K (over 195 K interval) is also more than 2 times larger than that ($\bar{\alpha}$ ~ -51.5×10^{-6}/K over a similar

View Article Online
DOI: 10.1039/C9MH01602C

interval of ~ 210 K) of the bonded $MnCo_{0.98}Cr_{0.02}Ge$.[29] Such a giant isotropic in-plane NTE in a wide temperature interval suggests the immense potential for compensating numerous materials with extremely high PTE, such as the widely-used organic or plastic materials, whose PTE coefficient is up to 100~200 × 10^{-6}/K.

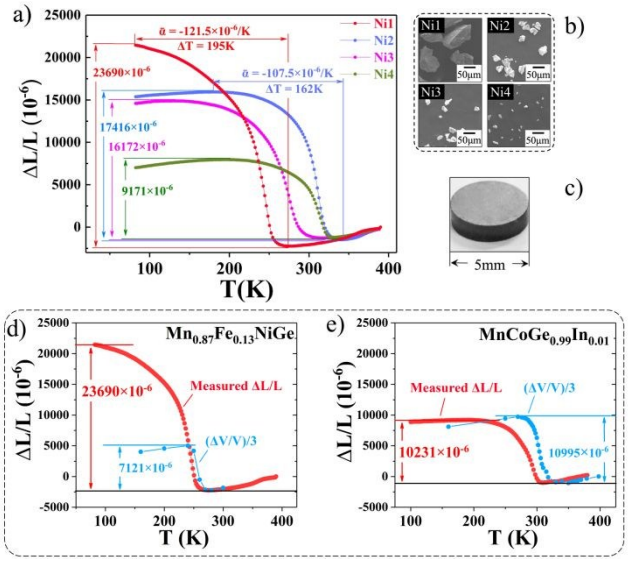

Fig. 3 a) The measured linear thermal expansions ΔL/L for the bonded $Mn_{0.87}Fe_{0.13}NiGe$ (Ni1), $MnNi_{0.8}Fe_{0.2}Ge$ (Ni2), $MnNi_{0.77}Fe_{0.23}Ge$ (Ni3), and $Mn_{0.91}Fe_{0.09}NiGe$ (Ni4) with different particle size (the reference temperature is 390 K). b) The SEM micrograph of particles before bonding. c) The morphology of the bonded particles. The comparison between the measured ΔL/L and the calculated $(\Delta L/L)_0$ = (ΔV/V)/3 for d) $Mn_{0.87}Fe_{0.13}NiGe$ and e) $MnCoGe_{0.99}In_{0.01}$.

To know the intrinsic crystallographic change during phase transition, we performed variable temperature NPD or XRD measurements for these Fe-doped MnNiGe alloys before bonding. The refined results are shown in Fig. S6 and Table S1. The changes of lattice volume ($\Delta V/V \sim (2V_H - V_O)/2V_H$) during phase transition at the corresponding same temperature point are -2.63%, -3.53%, -3.49%, and -2.66% for $Mn_{0.87}Fe_{0.13}NiGe$, $MnNi_{0.8}Fe_{0.2}Ge$, $MnNi_{0.77}Fe_{0.23}Ge$, and $Mn_{0.91}Fe_{0.09}NiGe$, respectively. If the lattice expansion was supposed to be isotropic for these polycrystalline samples, the linear $(\Delta L/L)_0$ = (ΔV/V)/3 from the unit cell parameters would be 7121, 7473, 7626, and 7190 × 10^{-6} in the temperature interval of 40K (240-280K), 35K (295-330K), 35K (275-310K), and 50K (285-335K), respectively (see supporting material III and Table S1). It is noticeable that the measured maximal ΔL/L for the bonded samples is 3.3, 2.3, 2.1, and 1.3 times larger than those calculated $(\Delta L/L)_0$ from crystallographic contribution for $Mn_{0.87}Fe_{0.13}NiGe$, $MnNi_{0.8}Fe_{0.2}Ge$, $MnNi_{0.77}Fe_{0.23}Ge$, and $Mn_{0.91}Fe_{0.09}NiGe$, respectively (Table S1). As a typical display, Fig. 3d shows the comparison between the measured ΔL/L and the calculated $(\Delta L/L)_0$=(ΔV/V)/3 for $Mn_{0.87}Fe_{0.13}NiGe$. In contrast, the measured ΔL/L for the bonded MnCoGe-based samples never exceeds the crystallographically calculated isotropic (ΔV/V)/3,[29] e.g., the maximal ΔL/L of $MnCoGe_{0.99}In_{0.01}$ is lower than 100% (~ 93%) of the crystallographic value (ΔV/V)/3 (Fig 3e) owing to the possibly introduced porosities during bonding process. The broadening of the NTE temperature range of the bonded samples compared to the free powders involving martensitic structural transition is ascribed to the introduced residual stress during molding process,[29] see details in supporting materials VI. For a single composition, similar enhancements of NTE are also demonstrated (supporting materials VII).

For the Fe-doped MnNiGe alloys, the introduced texture due to large lattice distortion should play a dominate role for the surprising giant NTE. To detect the degree of the introduced texture in the bonded samples with different particle sizes, we performed XRD measurements for the top surface of these bonded cylinders (Fig. 3c). Through comparing the diffraction patterns with those from free powders collected at room temperature, the degree of texture can be quantified.[40] Here we consider the Bragg peaks of the hexagonal structure in these diffraction patterns to calculate the orientation coefficient (OC) (see details in supporting material IV). The OC of each crystal plane ($h_ik_il_i$) can be calculated by Harris method[18] shown as below,

$$\mathrm{OC}\ (h_ik_il_i) = \frac{I(h_ik_il_i)/I_0(h_ik_il_i)}{(1/N)\cdot\sum_{j=1}^{N}[I(h_jk_jl_j)/I_0(h_jk_jl_j)]} \qquad (2)$$

where N is the number of the considered diffraction peaks (here N = 5, noting only 5 Bragg peaks from the hexagonal structure), $I_0(h_ik_il_i)$ is the peak intensity of ($h_ik_il_i$) crystal plane from free powders, and $I(h_ik_il_i)$ is the one from the top surface of bonded sample (Fig. 3c). This equation shows that the OC is determined by the intensity ratio of diffraction peaks from free powders and bonded pellets. For the free powders without orientation, OC = 1 for any crystal plane (Fig. 4a). If one crystal plane was fully orientated (Fig. 4b) (such as single crystal), OC = 5 for this plane, while OC = 0 for the other four. 1 < OC < 5 indicates partial orientation (Fig. 4c). From the calculated OCs (Table S1), it can be found that all the bonded MnNiGe with Fe doping have preferred orientations along (110) and (002) crystal plane. The OC (110) are 1.93, 1.69, 1.95, and 1.36, while the OC (002) are 1.23, 0.96, 1.40, and 1.22, for $Mn_{0.87}Fe_{0.13}NiGe$, $MnNi_{0.8}Fe_{0.2}Ge$, $MnNi_{0.77}Fe_{0.23}Ge$, and $Mn_{0.91}Fe_{0.09}NiGe$, respectively. In contrast, the OC is approaching 1 for all crystal planes of MnCoGeIn, indicating lack of preferred orientations (Table S1). In the hexagonal structure, the (110) plane is parallel to c-axis, while the (002) plane is perpendicular to c axis and parallel to a-axis (Fig. 4d). For Fe-doped MnNiGe (e.g. $Mn_{0.87}Fe_{0.13}NiGe$), the hexagonal lattice expands along c-axis by 12.01% and contracts along a-axis by 9.19% on cooling during the transition (Fig. S2). Clearly, the (110) orientation enhances the NTE while the (002) orientation reduces the NTE.

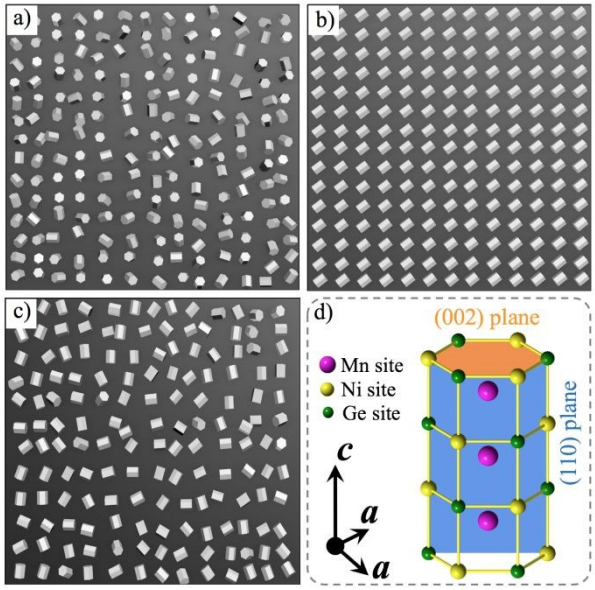

Fig. 4 The sketch of sample with different texture for the hexagonal structure (space group: $P6_3/mmc$). a) free powders without texture, OC = 1 for any crystal plane, b) fully orientated (110) plane with OC (110) =5, c) partially orientated (110) plane with 1 < OC (110) < 5, d) Schematic diagram of hexagonal lattice, where the (110) and (002) planes are denoted by blue and yellow, respectively.

To quantify the joint effect of the (110) and (002) orientations on the enhanced ΔL/L (compared to the crystallographic value $(\Delta L/L)_0$), a numerical simulation was performed (see details in supporting material V), and the result is three-dimensionally plotted in Fig. 5 and Fig. S8b. It can be discerned that all the experimental points roughly fall on the simulated curves. As the OC (002) = 1 was fixed, the OC (110) orientation would dominate the thermal expansion, and the $(\Delta L/L)/(\Delta L/L)_0$ increases monotonously with varying OC(110), as shown in Fig. 5, implying the large enhancement of NTE. As for the $MnCoGe_{0.99}In_{0.01}$ alloy lacking preferred orientation, the OC is approaching 1 for any crystal plane (Table S1), and the experimental $(\Delta L/L)/(\Delta L/L)_0$ is smaller than 1 (~ 0.93).[29] Obviously, it is more difficult to introduce texture into $MnCoGe_{0.99}In_{0.01}$ compared to Fe-doped MnNiGe. The crucial cause lies in the different lattice distortion owing to the distinct magnetic structure in martensite for the two alloys.

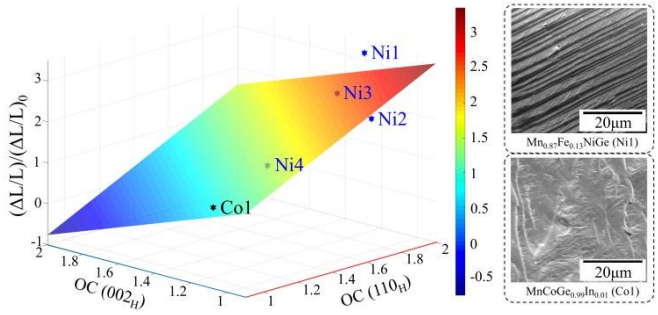

Fig. 5 Left panel: the functional plane drawn according to numerical simulation, where the OC (110), OC (002), and $(\Delta L/L)/(\Delta L/L)_0$ are set as x, y and z, respectively. Stars denote the experimental points for $Mn_{0.87}Fe_{0.13}NiGe$ (Ni1), $MnNi_{0.8}Fe_{0.2}Ge$ (Ni2), $MnNi_{0.77}Fe_{0.23}Ge$ (Ni3), $Mn_{0.91}Fe_{0.09}NiGe$ (Ni4), and $MnCoGe_{0.99}In_{0.01}$ (Co1). Right panel: The typical comparison of SEM micrographs between $Mn_{0.87}Fe_{0.13}NiGe$ (Ni1) and $MnCoGe_{0.99}In_{0.01}$ (Co1) bulk.

MnNiGe alloys with different Fe doping in present work show similar lattice distortion owing to their similar cone-spiral magnetic structure (see supporting material II, Fig. S3, S4 and S5). But their average particle sizes before bonding are different, i.e., 60~80 μm, 20~50 μm, 20~40 μm, and 10~20 μm for $Mn_{0.87}Fe_{0.13}NiGe$, $MnNi_{0.8}Fe_{0.2}Ge$, $MnNi_{0.77}Fe_{0.23}Ge$, and $Mn_{0.91}Fe_{0.09}NiGe$, respectively. Generally, the degree of texture diminishes with reducing particle size. This rule also works in present work. One can notice the positive correlation between the NTE and the particle size (Fig. 3a,b).

Theoretically, during the process of phase transition accompanied by significant lattice distortion, cracks produce inside the grains in addition to the dislocations at the grain boundaries. The produced cracks inside the grains must be positively correlated with the degree of lattice distortion during phase transition. The larger the distortion, the more cracks appear in the grains. With the assistance of massive cracks, materials with large distortion prefer cleavage breaking.[41] Right panel of Fig. 5 shows the comparison of the SEM images of fracture surface between the bulk $Mn_{0.87}Fe_{0.13}NiGe$ (Ni1) and $MnCoGe_{0.99}In_{0.01}$ (Co1). For the former, clear texture forms along the cleavage plane owing to the larger lattice distortion. While for the latter, the less lattice distortion is not enough to produce enough cracks to motivate the cleavage breaking. Hence the $MnCoGe_{0.99}In_{0.01}$ tends to randomly break and no obvious texture appears.

During the cleavage process, the cracks tend to cleave the crystal by propagating in the cleavage planes. In the Griffith model,[41] for a crack with length c, the critical stress σ to expand the crack is denoted by equation $\sigma = \{(2\gamma E)/(\pi c)\}^{1/2}$, where the Young's modulus E is related to atomic bond strength. Thus, the critical stress σ is proportional to the surface energy γ of cleaved plane and positively correlates with the bond strength wherein. In a hexagonal crystal, the cleavage planes parallel to [001] direction, i.e. c-axis, have relatively low energy and weak bond strength,[41] hence the hexagonal crystal tends to cleave along c-axis. Moreover, the c-axis prefers to lie down under physical pressure during molding process (Fig. 4b, c, and d). As a result, controlled texture effect appears and large enhancement of linear ΔL/L occurs.

Conclusions

By utilizing the large lattice distortion caused by incommensurate cone-spiral magnetic ordering and the constructed texture during molding process, giant NTE exceeding average crystallographical contribution has been realized in Fe-doped MnNiGe alloys. The maximal ΔL/L ~ 23690 × 10^{-6} and the corresponding NTE coefficient $\tilde{\alpha}$ ~ -121.5 × 10^{-6}/K over a wide interval ~195 K (80-275K) were observed, which is 3.3 times larger than that of corresponding average crystallographical contribution. Neutron powder diffractions and first-principle calculations disclose the incommensurate

cone-spiral magnetic ordering in Fe-doped MnNiGe, which produces large lattice distortion during phase transition and motivates the cleavage breaking of hexagonal phase along c-axis. As a result, controlled texture effect along (110) crystal plane appears, which greatly enhances the in-plane isotropic linear ΔL/L. The fundamental advance by utilizing the magnetic structure controlled lattice distortion and the induced texture effect to gain giant NTE paves a new way for exploring NTE materials, which is of great significance for developing novel NTE materials to meet various desires in modern industries, particularly for compensating the materials with extremely high PTE coefficient, such as the widely-used organic or plastic materials.

Conflicts of interest

There are no conflicts to declare.

Acknowledgements

This work was supported by the National Basic Research Program of China (2017YFB0702702, 2017YFA0206300, 2018YFA0305704), the National Natural Sciences Foundation of China (U1832219, 51531008, 51771223, 51590880), and the Key Research Program of the Chinese Academy of Sciences.

Author contributions

F.X.H., Q.Z.H., L.H.H. and B.G.S. conceived the study. The first two authors F.R.S. and H.B.Z. contribute equally to this work. F.R.S., H.B.Z., F.X.L. and Z.B.Y prepared the samples and measured the NTE. Q.Z.H., L.H.H., F.R.S., H.W., J.C. and T.J.L. performed NPD measurements and analysis. J.T.W., S.H.D. and B.T.W. performed DFT calculations. F.R.S., H.B.Z. and J.Z.H. performed magnetic, XRD and SEM measurements. All authors contributed to the analysis and discussion. F.X.H., F.R.S. and J.W. wrote and edited the paper. J.R.S. and B.G.S. made valuable comments on the paper.

Notes and references

1 J. Chen, L. Hu, J. X. Deng and X. R. Xing, *Chem. Soc. Rev.,* 2015, **44,** 3522-3567.
2 T. A. Mary, J. S. O. Evans, T. Vogt and A. W. Sleight, *Science,* 1996, **272,** 90-92.
3 J. S. O. Evans, T. A. Mary, T. Vogt, M. A. Subramanian, A. W. Sleight, *Chem. Mater.,* 1996, **8,** 2809-2823.
4 J. Chen, Q. L. Gao, A. Sanson, X. X. Jiang, Q. Z. Huang, A. Carnera, C. G. Rodriguez, L. Olivi, L. Wang, L. Hu, K. Lin, Y. Ren, Z. S. Lin, C. Wang, L. Gu, J. X. Deng, J. P. Attfield and X. R. Xing, *Nat. Commun.,* 2017, **8,** 14441.
5 L. Hu, J. Chen, A. Sanson, H. Wu, C. G. Rodriguez, L. Olivi, Y. Ren, L. L. Fan, J. X. Deng and X. R. Xing. *J. Am. Chem. Soc.,* 2016, **138,** 8320-8323.
6 L. Hu, J. Chen, L. L. Fan, Y. Ren, Y. C. Rong, Z. Pan, J. X. Deng, R. B. Yu and X. R. Xing, *J. Am. Chem. Soc.,* 2014, **136,** 13566-13569.
7 J. Chen, X. R. Xing, G. R. Liu, J. H. Li, Y. T. Liu, *Appl. Phys. Lett.,* 2006, **99,** 101914.
8 J. Chen, X. R. Xing, C. Sun, P. H. Hu, R. B. Yu, X. W. Wang and L. H. Li, *J. Am. Chem. Soc.,* 2008, **130,** 1144-1145.
9 P. H. Hu, J. Chen, J. X. Deng and X. R. Xing, *J. Am. Chem. Soc.,* 2010, **132,** 1925-1928.
10 K. Takenaka and H. Takagi, *Appl. Phys. Lett.,* 2005, **87,** 261902.
11 S. H. Deng, Y. Sun, H. Wu, Q. Z. Huang, J. Yan, K. W. Shi, M. I. Malik, H. Q. Lu, L. Wang, R. J. Huang, L. F. Li and C. Wang, *Chem. Mater.* 2015, **27,** 2495-2501.
12 C. Wang, L. H. Chu, Q. R. Yao, Y. Sun, M. M. Wu, L. Ding, J. Yan, Y. Y. Na, W. H. Tang, G. N. Li, Q. Z. Huang and J. W. Lynn, *Phys. Rev. B,* 2012, **85,** 220103.
13 Y. Sun, C. Wang, Y. C. Wen, L. H. Chu, H. Pan and M. Nie, *J. Am. Ceram. Soc.,* 2010, **93,** 2178-2181.
14 P. Tong, D. Louca, G. King, A. Llobet, J. C. Lin and Y. P. Sun, *Appl. Phys. Lett.,* 2013, **102,** 041908.
15 S. P. Li, R. J. Huang, Y. Q. Zhao, W. Wang, Y. M. Han and L. F. Li *Adv. Funct. Mater.,* 2017, **27,** 1604195.
16 R. J. Huang, Y. Y. Liu, W. Fan, J. Tan, F. R. Xiao, L. H. Qian and L. F. Li, *J. Am. Chem. Soc.,* 2013, **135,** 11469-11472.
17 Y. Z. Song, J. Chen, X. Z. Liu, C. W. Wang, J. Zhang, H. Liu, H. Zhu, L. Hu, K. Lin, S. T. Zhang and Xing, X. R. *J. Am. Chem. Soc.,* 2018, **140,** 602–605.
18 M. Azuma, W. T. Chen, H. Seki, M. Czapski, S. Olga, K. Oka, M. Mizumaki, T. Watanuki, N. Ishimatsu, N. Kawamura, S. Ishiwata, M. G. Tucker, Y. Shimakawa and J. P. Attfield, *Nat. Commum.,* 2011, **2,** 347.
19 X. G. Zheng, H. Kubozono, H. Yamada, K. Kato, Y. Ishiwata and C. N. Xu, *Nat. Nanotechnol.,* 2008, **3,** 724-726.
20 J. Chen, L. L. Fan, Y. Ren, Z. Pan, J. X. Deng, R. B. Yu and X. R. Xing, *Phys. Rev. Lett.,* 2013, **110,** 115901.
21 X. Y. Song, Z. H. Sun, Q. Z. Huang, M. Rettenmayr, X. M. Liu, M. Seyring, G. N. Li, G. H. Rao and F. X. Yin, *Adv. Mater.,* 2011, **23,** 4690–4694.
22 Q. Li, H. Zhu, L. R. Zheng, L. L. Fan, N. Wang, Y. C. Rong, Y. Ren, J. Chen, J. X. Deng and X. R. Xing, *Nano Lett.,* 2017, **17,** 7892–7896.
23 Q. Li, H. Zhu, L. R. Zheng, L. L. Fan, Y. Ren, J. Chen, J. X. Deng and X. R. Xing, *Adv. Sci.,* 2016, **3,** 1600108.
24 H. Zhu, Q. Li, Y. Ren, L. L. Fan, J. Chen, J. X. Deng and X. R. Xing, *Adv. Mater.,* 2016, **28,** 6894-6899.
25 L. Hu, F. Y. Qin, A. Sanson, L. F. Huang, Z. Pan, Q. Li, Q. Sun, L. Wang, F. M. Guo, U. Aydemir, Y. Ren, C. J. Sun, J. X. Deng, G. Aquilanti, J. M. Rondinelli, J. Chen and X. R. Xing, *J. Am. Chem. Soc.,* 2018, **140,** 4477–4480.
26 T. F. Qi, O. B. Korneta, S. Parkin, L. E. De Long, P. Schlottmann and G. Cao, *Phys. Rev. Lett.,* 2010, **105,** 177203.
27 K. Takenaka, Y. Okamoto, T. Shinoda, N. Katayama and Y. Sakai, *Nat. Commum.,* 2017, **8,** 14102.
28 V. Johnson, *Inorg. Chem.,* 1975, **14,** 1117-1120.
29 Y. Y. Zhao, F. X. Hu, L. F. Bao, J. Wang, H. Wu, Q. Z. Huang, R. R. Wu, Y. Liu, F. R. Shen, H. Kuang, M. Zhang, X. Q. Zheng, J. R. Sun and B. G. Shen, *J. Am. Chem. Soc.,* 2015, **137,** 1746-1749.
30 R. R. Wu, L. F. Bao, F. X. Hu, H. Wu, Q. Z. Huang, J. Wang, X. L. Dong, G. N. Li, J. R. Sun, F. R. Shen, T. Y. Zhao, X. Q. Zheng, L. C. Wang, Y. Liu, W. L. Zuo, Y. Y. Zhao, M. Zhang, X. C. Wang, C. Q. Jin, G. H. Rao, X. F. Han and B. G. Shen, *Sci. Rep.,* 2015, **5,** 18027.
31 S. Anzai and K. Ozawa, *Phys. Rev. B,* 1978, **18,** 2173-2178.
32 Z. Gercsi and K. G. Sandeman, *Phys. Rev. B,* 2010, **81,** 224426.
33 Z. Gercsi, K. Hono and K. G. Sandeman, *Phys. Rev. B,* 2011, **83,** 174403.
34 W. Bazela, A. Szytula, J. Todorovic, Z. Tomkowicz and A. Zieba, *Phys. Status Solidi A,* 1976, **38,** 721.
35 A. Szytula, A. T. Pedziwiatr, Z. Tomkowicz and W. Bazela, *JMMM.,* 1981, **25,** 176-186.

View Article Online
DOI: 10.1039/C9MH01602C

36 E. K. Liu, W. H. Wang, L. Feng, W. Zhu, G. J. Li, J. L. Chen, H. W. Zhang, G. H. Wu, C. B. Jiang, H. B. Xu and D. B. Frank, *Nat. Commun.,* 2012, **3,** 873.
37 W. Bazela, A. Szytula, J. Todorovic and A. Zieba, *Phys. Status Solidi A,* 1981, **64,** 367-378
38 J. P. Perdew, Y. Wang, *Phys. Rev. B: Condens. Matter Mater. Phys.,* 1992, **45,** 13244−13249.
39 S. H. Deng, Y. Sun, L. Wang, Z. X. Shi, H. Wu, Q. Z. Huang, J. Yan, K. W. Shi, P. W. Hu, A. Zaoui and C. Wang, *J. Phys. Chem. C,* **2015,** 119, 24983-24990
40 G. B. Harris, *Philos. Mag.,* 1952, **43,** 113-123.
41 B. Siemens, C. Domke, Ph. Ebert and K. Urban, *Phys. Rev. B,* 1999, **59,** 3000-3007.

View Article Online
DOI: 10.1039/C9MH01602C

For Table of Contents Only

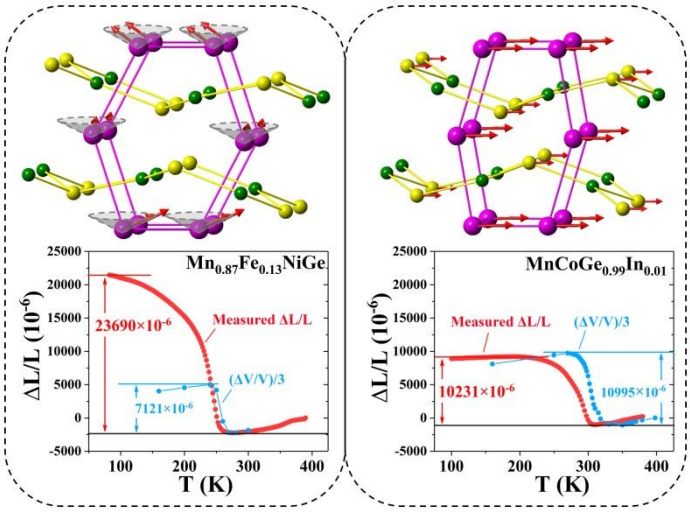

By utilizing the large lattice distortion caused by incommensurate cone-spiral magnetic ordering and the induced texture effect in Fe-doped MnNiGe alloys, NTE largely exceeding average crystallographical contribution has been achieved.